

# Supplementary Information

## Growth Mechanism of Chevron Graphene Nanoribbons on (111)-Oriented Coinage Metal Surfaces

Elie Geagea<sup>1</sup>, Daniel Medina-Lopez<sup>2</sup>, Luca Giovanelli<sup>1</sup>, Laurent Nony<sup>1</sup>, Christian Loppacher<sup>1</sup>,  
Stéphane Campidelli<sup>2</sup>, Sylvain Clair<sup>1,\*</sup>

<sup>1</sup> *Aix Marseille University, CNRS, IM2NP, 13013 Marseille, France*

<sup>2</sup> *Université Paris-Saclay, CEA, CNRS, NIMBE, LICSEN, 91191, Gif-sur-Yvette, France*

\*Corresponding author: [sylvain.clair@cnrs.fr](mailto:sylvain.clair@cnrs.fr)

### Table of Contents

Additional STM images .....	S2
Kinetic Monte Carlo Simulations .....	S9
Methods.....	S12
References .....	S15

## Additional STM images

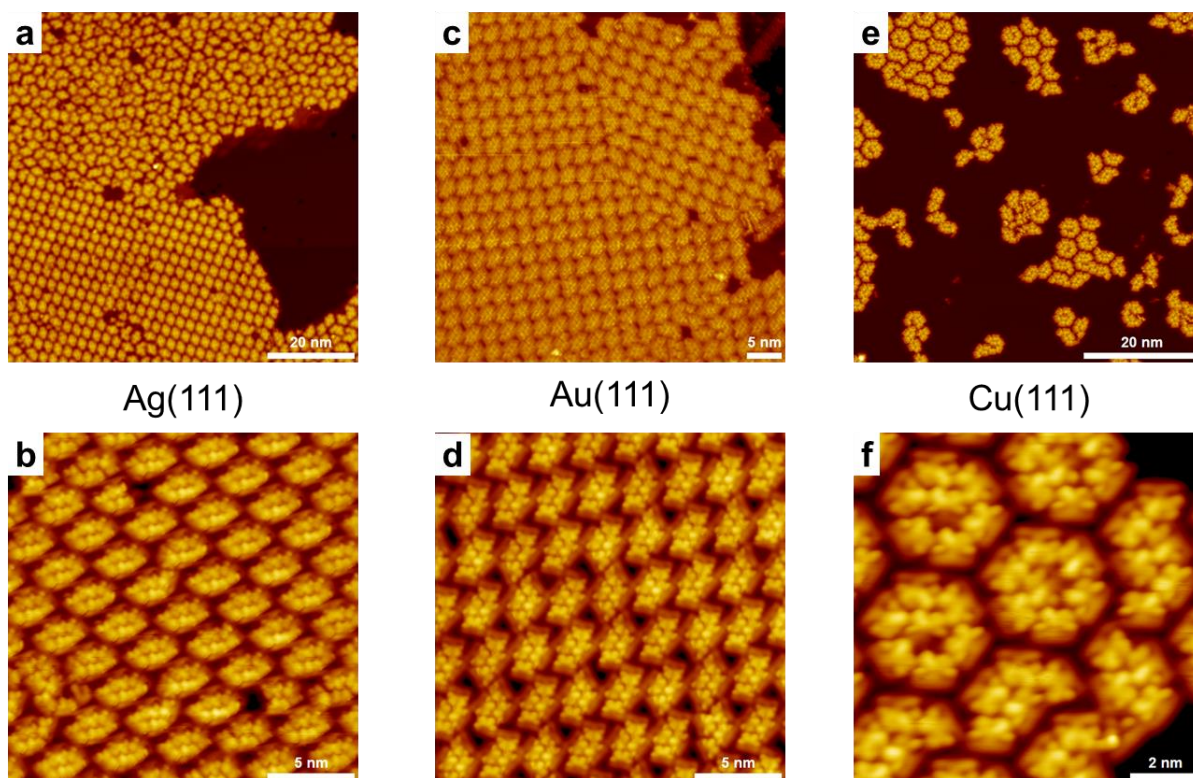


Fig. S1. STM images of the supramolecular phases obtained after deposition of **1** at room temperature (a,b) on Ag(111) and (c,d) on Au(111), and (e,f) after deposition at low temperature (-80 °C) on Cu(111). The phases consist in the formation of small islands comprising 4 to 7 molecules, see Ref. <sup>1</sup> for details.

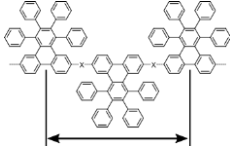
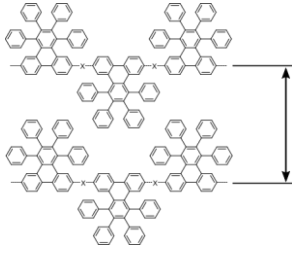
	 Intrachain periodicity	 Interchain distances
Organometallic chain - excepted Au(111)	$2.22 \pm 0.05$ (Figs. 2, S2) $2.3 \pm 0.1$ <sup>2</sup>	$1.85 \pm 0.05$ (Figs. 2, S2) $1.62 \pm 0.05$ (Figs. 2, S2) $1.32 \pm 0.05$ (Figs. 2, S2)
Covalent polymer	$1.70 \pm 0.05$ (Fig. 3) $1.7 \pm 0.1$ <sup>2</sup> $1.6$ <sup>3</sup>	$1.65 \pm 0.05$ (Fig. 3) $1.90 \pm 0.05$ (Fig. 3)
GNR	$1.70 \pm 0.05$ (Figs. 5, S4, S6) $1.70$ <sup>4</sup> $1.77$ <sup>5</sup> $1.704$ <sup>6</sup> $1.71$ <sup>7</sup>	repulsive

Table S1. Summary of the distances (in nm) measured in the STM images for the different phases and compared with those from the literature.

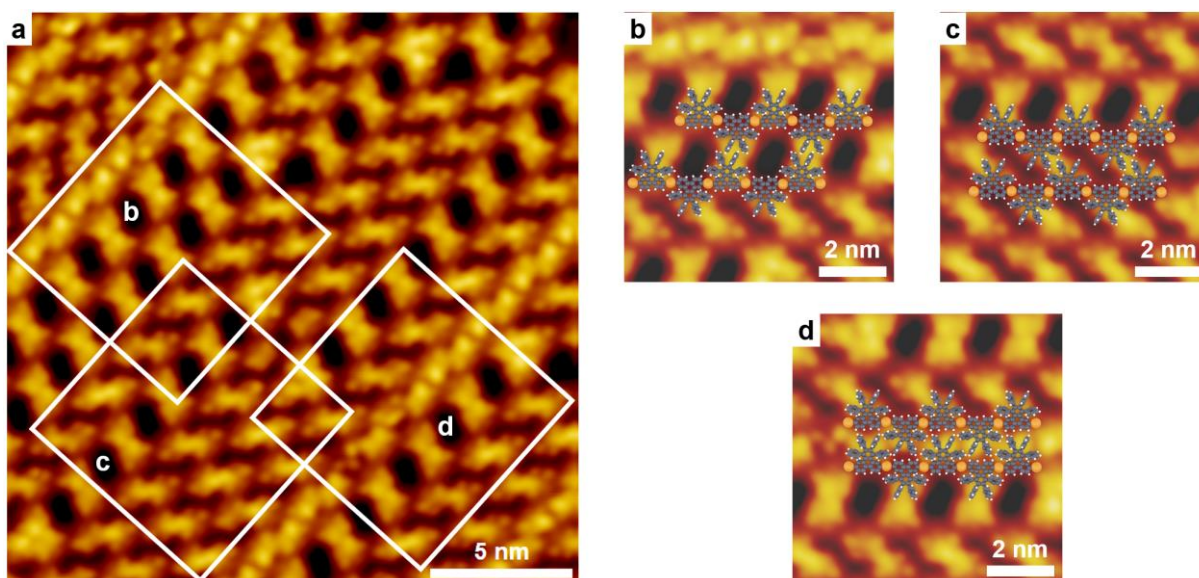


Fig. S2. STM images of the organometallic chains obtained on Ag(111) after annealing at 200 °C. (a) STM image representing the three distinct modes of 2D self-assembly highlighted with three white inspection areas corresponding to: (b,c) The two nanoporous configurations driven mainly by  $\pi$ - $\pi$  interactions between the two phenyls labelled 2 and 3; (d) A more compact configuration resulting from an important chain intertwining and  $\pi$ - $\pi$  interactions involving all four phenyls. Each interchain configuration is represented by a model superimposed on the STM images (scaled but not computationally relaxed). Carbon atoms: dark grey; Hydrogen atoms: white; Silver adatoms: yellow.

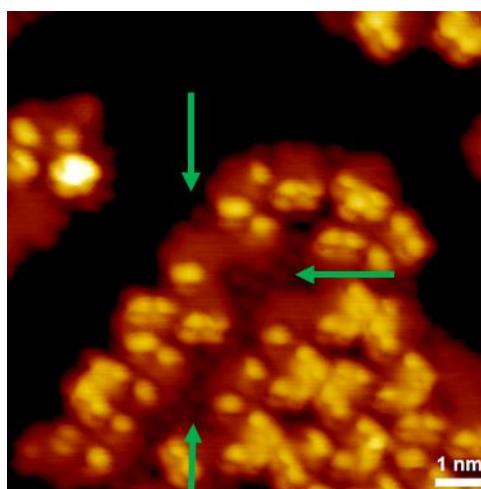


Fig. S3. STM image obtained on Cu(111) after long annealing at 230 °C to initiate intermediate cyclodehydrogenation. The Br atoms are visible in the vicinity of the GNR, as shown by the green arrows.

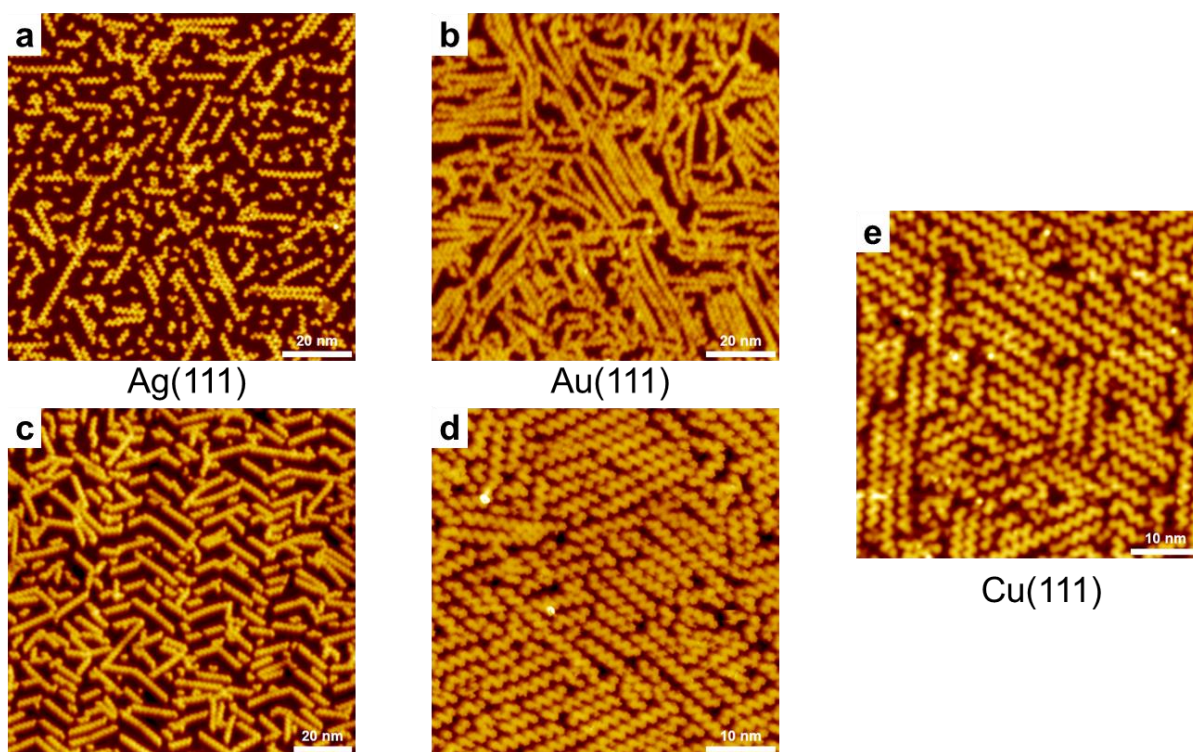


Fig. S4. STM images of chevron GNR obtained for different depositions on (a,c) Ag(111), (b,d) Au(111) and (e) Cu(111). Most of the GNRs are well separated from each other, signaling a long-range repulsive interaction between the ribbons. Annealing temperatures: (a) 400 °C, (b-d) 450 °C, (e) 300 °C.

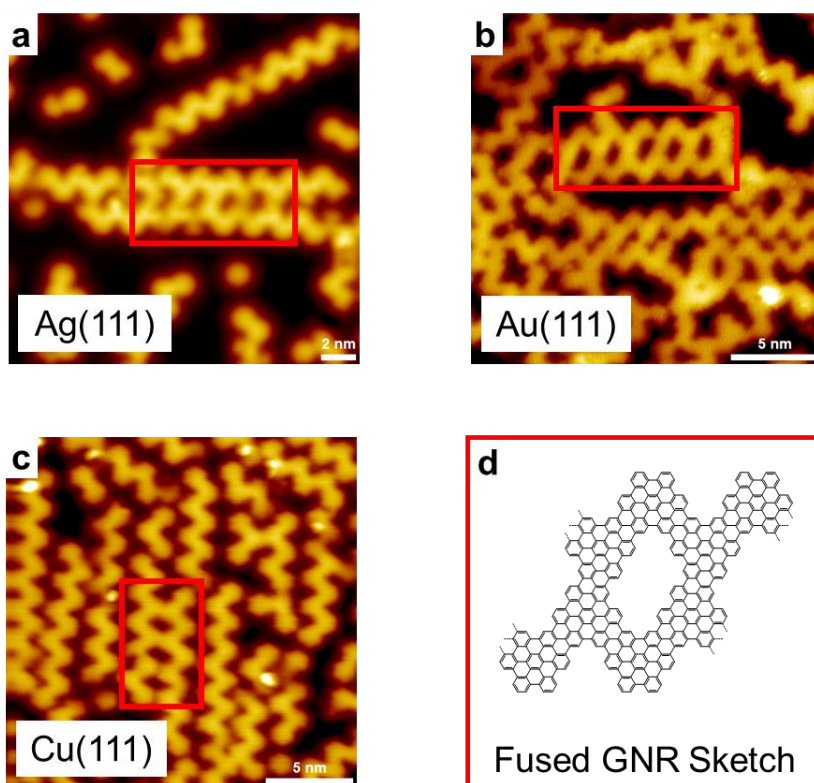


Fig. S5. STM images of some portions of adjacent cGNR that are locally fused after annealing at (a) 400 °C on Ag(111), (b) 550 °C on Au(111) and (c) 300 °C on Cu(111).

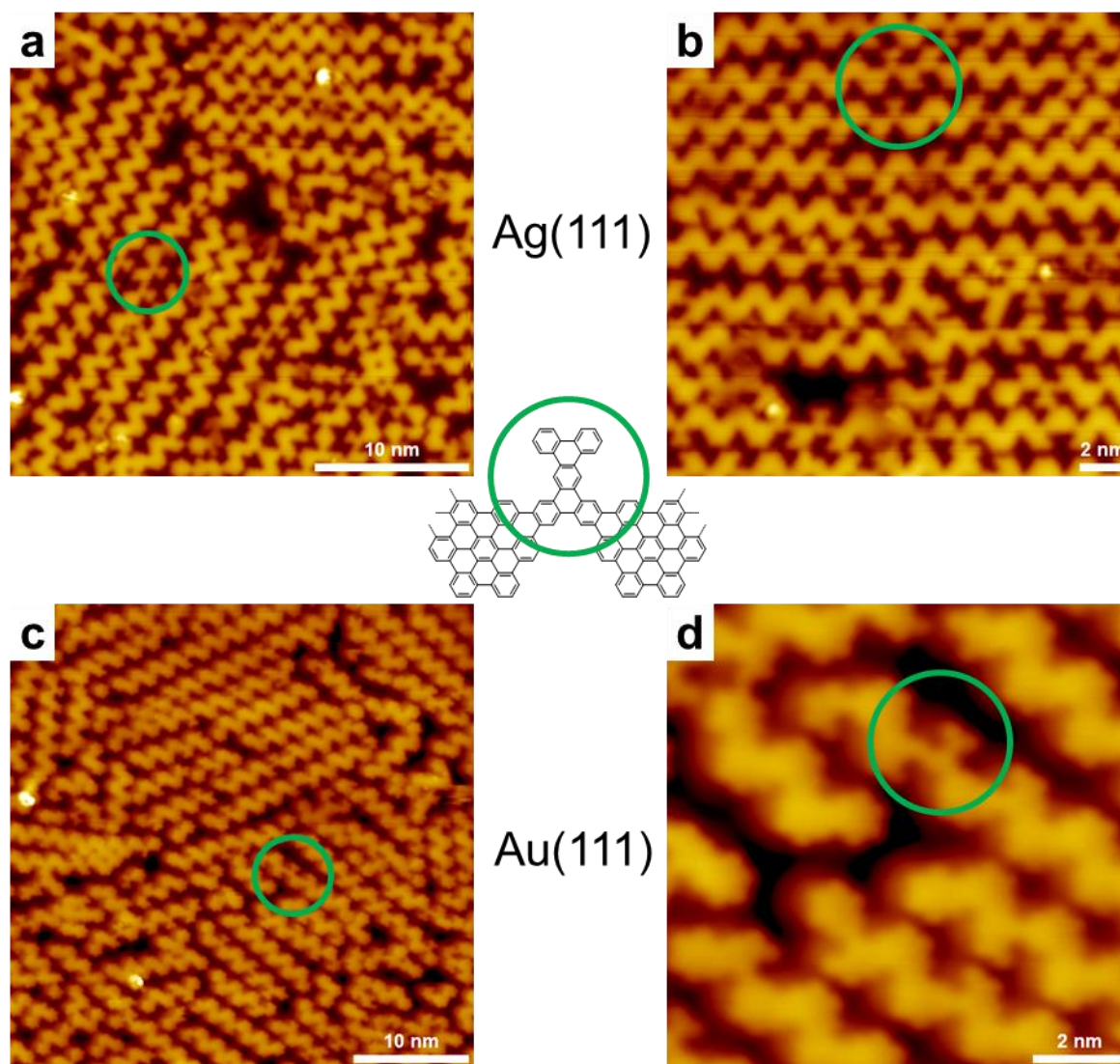


Fig. S6. STM images of the typical defects (some of them highlighted in green circles) that can be observed after cGNR formation at high coverage on (a,b) Ag(111) and (c,d) Au(111). As shown in the central sketch, these defects correspond to the loss of the two phenyls labelled 1 and 4 (see main text Fig. 1b). No such defect was observed on Cu(111).

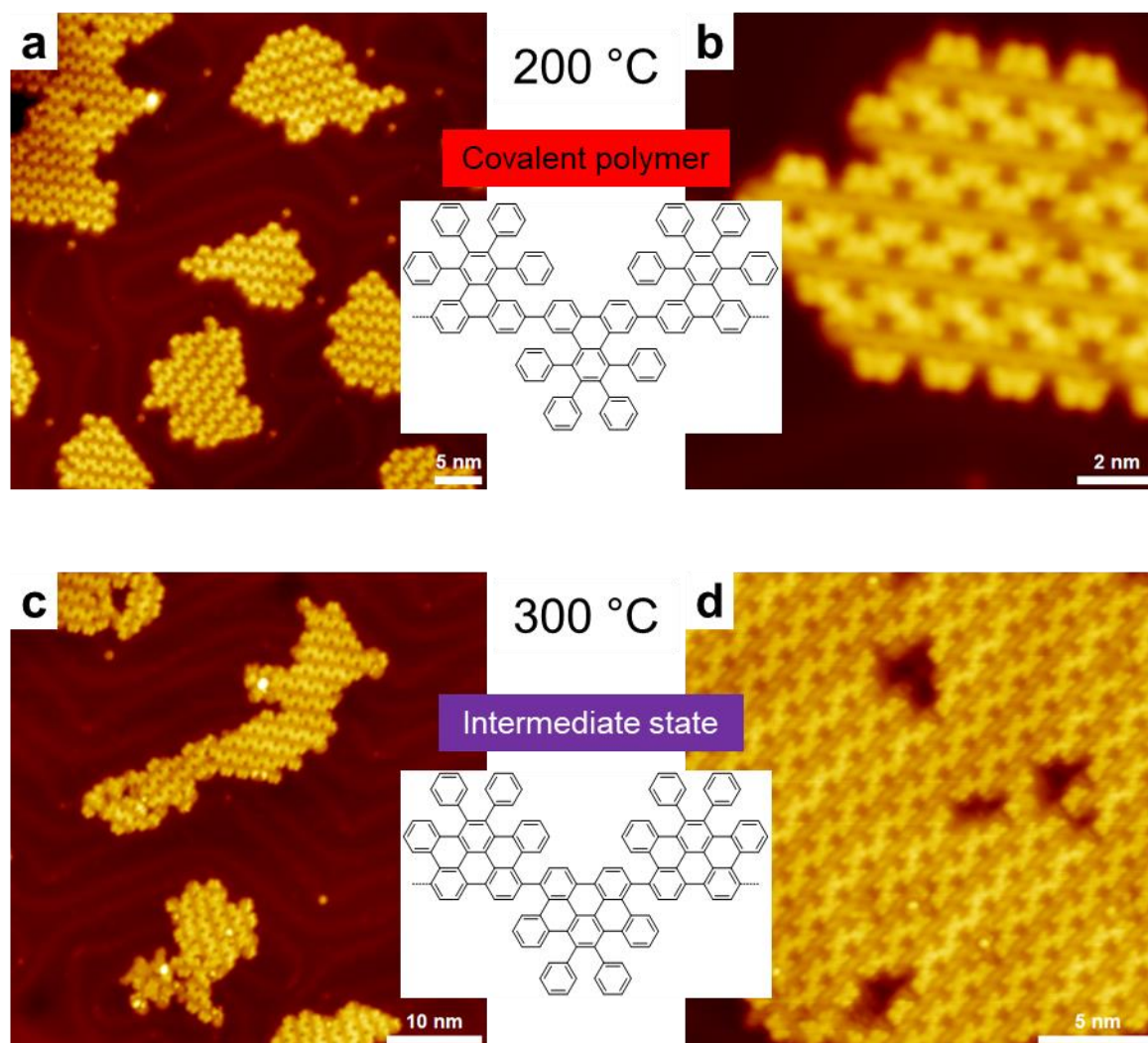


Fig. S7. STM images of the structures obtained on Au(111) after annealing at (a,b) 200 °C (covalent polymer) and at (c,d) 300 °C (intermediate state). Although the intermediate state is partially dehydrogenated, no difference in the STM contrast and the domain organization can be observed between both types.



## **Kinetic Monte Carlo Simulations**

The cyclodehydrogenation processes leading to HBr and H<sub>2</sub> desorption were simulated by a simple model using a Kinetic Monte Carlo method implemented in CARLOS program.<sup>8,9</sup> Phenyl-hydrogens and Br atoms were regularly distributed in a 2:1 ratio on a hexagonal 256×256 lattice and the temperature was linearly varied from 370 K to 720 K with a heating rate of 20 K.min<sup>-1</sup>. The phenyl-hydrogens were independently allowed to transform to atomic hydrogens, to simulate the dehydrogenation reaction. An atomic H and a neighboring atomic Br (respectively H) could transform into HBr (resp. H<sub>2</sub>) and desorb. The activation barrier for H<sub>2</sub> desorption was taken as  $E_{H_2} = 66.2 \text{ kJ.mol}^{-1} \approx 0.686 \text{ eV}$ , as estimated in Ref.<sup>10</sup>. The calculations were run with input energies implemented in kJ.mol<sup>-1</sup>.

The Br atoms were not diffusing (because in the real system they are trapped under the precursors), and the H atoms were diffusing on the lattice with an artificially high activation barrier of  $100 \text{ kJ.mol}^{-1} \approx 1.04 \text{ eV}$ , representing a sufficiently low value to allow an extensive exploration of the whole lattice sites, but also sufficiently high to limit the computational time. The attempt frequency for all processes (dehydrogenation, diffusion and desorption) was  $10^{13} \text{ Hz}$ .

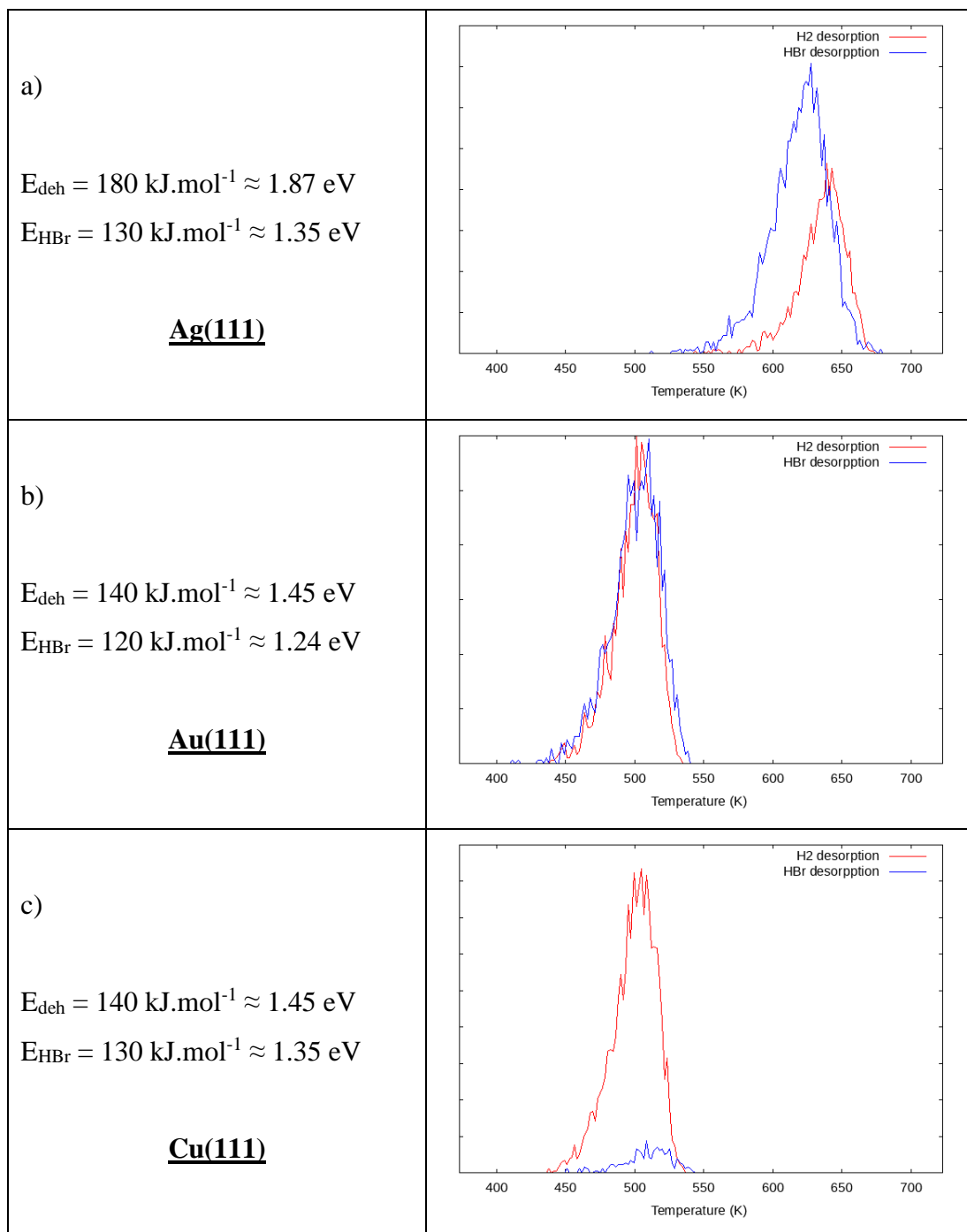
The activation barriers for dehydrogenation ( $E_{\text{deh}}$ ) and HBr desorption ( $E_{\text{HBr}}$ ) were adjusted to reproduce the experimental results of Fig. 6 in the main manuscript text. The results are presented below in Fig. S8a-c. The overlap between the HBr and H<sub>2</sub> desorption peaks observed in TDS for Ag(111) around 650 K (380 °C) could be well reproduced (Fig. S8a and Fig. 6a), as well as the perfect overlap between both peaks around 520 K (250 °C) observed for Au(111) (Fig. S8b and Fig. 6b).

The simulation thus indicates a dehydrogenation activation energy ( $E_{\text{deh}}$ ) of  $180 \text{ kJ.mol}^{-1} \approx 1.87 \text{ eV}$  ( $140 \text{ kJ.mol}^{-1} \approx 1.45 \text{ eV}$ ) on Ag(111) (Au(111), respectively), to be compared with  $150 \text{ kJ.mol}^{-1} \approx 1.55 \text{ eV}$  that was estimated for another precursor on Au(111).<sup>11</sup>

Also, the simulations suggest an increased stability of bromine in its adsorbed configuration under the precursor, providing an activation barrier for HBr desorption as high as  $130 \text{ kJ.mol}^{-1} \approx 1.35 \text{ eV}$  on Ag(111) and  $120 \text{ kJ.mol}^{-1} \approx 1.24 \text{ eV}$  on Au(111). These values can be compared with the DFT estimated value of  $68.5 \text{ kJ.mol}^{-1} \approx 0.710 \text{ eV}$  on bare Au(111).<sup>10</sup>

Fig. S8c presents the simulation results obtained with a low dehydrogenation barrier, providing a desorption peak around 520 K similar to the Au(111) case, and with a high activation energy for HBr desorption. In such a case, the HBr desorption peak is almost absent and all hydrogens desorb in the form of H<sub>2</sub>, leaving Br atoms intact on the surface. Such situation is representative of the case experimentally observed for Cu(111) (Fig. 6c). Note that, for  $E_{\text{HBr}} = 130 \text{ kJ.mol}^{-1} \approx 1.35 \text{ eV}$ , yet a very small fraction of Br has desorbed. Any value for  $E_{\text{HBr}}$  larger than 1.3 eV would then give qualitatively the same result, and the simulation can thus provide a lower limit only for this parameter.

Fig. S8d presents the simulation results obtained with a high dehydrogenation barrier, providing a desorption peak around 650 K similar to the Ag(111) case, but with a low activation energy for HBr desorption. In such case, the HBr and H<sub>2</sub> desorption peaks are perfectly separated, similar to what was observed in previous publications for aGNR and other precursors.<sup>10-12</sup>



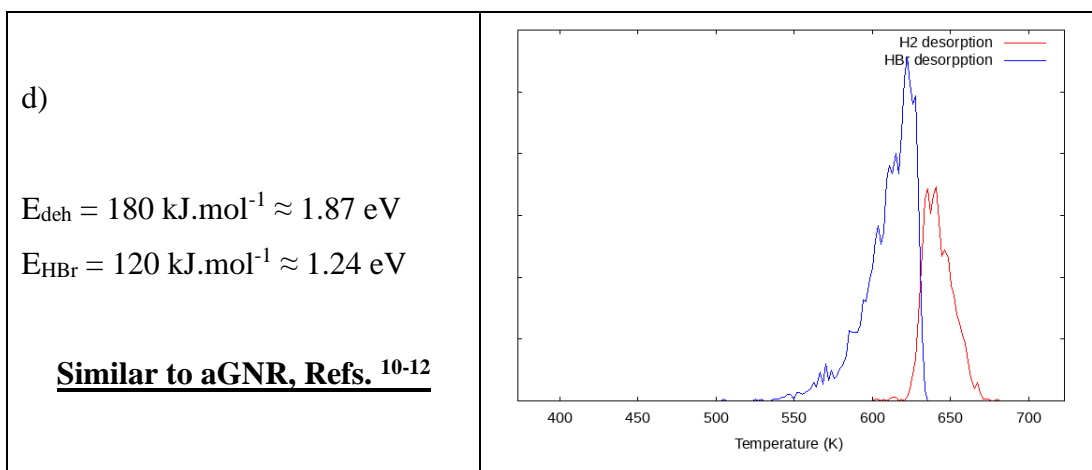


Fig. S8. Kinetic Monte Carlo simulations of the thermal desorption process with different activation energies implemented for the dehydrogenation reaction ( $E_{\text{deh}}$ ),  $\text{H}_2$  desorption ( $E_{\text{H}_2}$ ) and  $\text{HBr}$  desorption ( $E_{\text{HBr}}$ ) processes. These parameters were adjusted to reproduce the experimental results of Fig. 6 in the main manuscript text. The diffusion barriers were taken as  $100 \text{ kJ.mol}^{-1} \approx 1.04 \text{ eV}$  for  $\text{H}_2$  and infinite for  $\text{Br}$ . The  $\text{H}_2$  desorption activation energy ( $E_{\text{H}_2}$ ) was taken as  $E_{\text{H}_2} = 66.2 \text{ kJ.mol}^{-1} \approx 0.686 \text{ eV}$ .<sup>10</sup>

## Methods

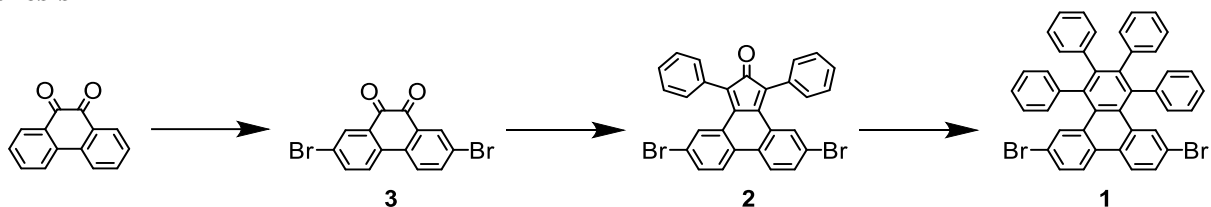
### Techniques

NMR spectra were recorded with a Bruker Avance Neo 400 (400 MHz) instrument, with the solvent used as an internal reference. MALDI-TOF mass spectra were recorded on a Bruker Autoflex speed; the samples were analyzed in DCTB (*trans*-2-[3-(4-*tert*-butylphenyl)-2-methyl-2-propenylidene]malononitrile) matrix. Thin layer chromatography (TLC) was performed on silica gel 60 F254 (Merck) precoated aluminum sheets. Column chromatography was performed on Merck silica gel 60 (0.063-0.200 mm) or puriFlash® Si-HP 60 Å 15 or 30 µm columns with an Interchim puriFlash 430.

### Materials

Chemicals were purchased from Aldrich or Fisher Scientific and were used as received. Solvents were purchased from SDS Carlo Erba, Aldrich or Fisher Scientific and were used as received. The GNR precursor **1** (6,11-dibromo-1,2,3,4-tetraphenyltriphenylene)<sup>4</sup> was synthesized according to the literature procedure.<sup>13,14</sup>

### Synthesis



#### 2,7-dibromophenanthrene-9,10-dione (**3**).<sup>13</sup>

Phenanthrene-9,10-dione (3.5 g, 16 mmol) was dissolved in concentrated sulfuric acid (96 mL). *N*-bromosuccinimide (6.43 g, 36 mmol) was added to the mixture, and the reaction was stirred at room temperature overnight. The solution was added to water (200 mL). The bright orange powder was recovered by Büchner filtration, and then recrystallized in dimethyl sulfoxide to yield the product as an orange powder (4.68 g, 79% yield). <sup>1</sup>H NMR (400 MHz, DMSO-*d*<sub>6</sub>, 298 K): δ(ppm) 8.26 (s, 2H), 8.17 – 7.86 (m, 4H).

#### 5,10-dibromo-1,3-diphenyl-2H-cyclopenta[1]phenanthren-2-one (**2**).<sup>13</sup>

2,7-dibromophenanthrene-9,10-dione **3** (2.4 g, 6.6 mmol), diphenylacetone (1.8 g, 8.60 mmol) were dissolved in methanol (46 mL). The mixture was heated to 80 °C and potassium hydroxide (388 mg, 6.93 mmol), previously dissolved in methanol (20 mL), was added to the mixture dropwise. The reaction was heated for 2 h then cooled down in an ice bath. The formed precipitate was filtered and recrystallized in methanol and chloroform. The cyclopentadienone **2** was recovered as a green powder (1.09 g, 30% yield).

$^1\text{H}$  NMR (400 MHz,  $\text{CDCl}_3$ , 298 K):  $\delta$ (ppm) 7.66 (d,  $J = 2.1$  Hz, 2H), 7.61 (d,  $J = 8.6$  Hz, 2H), 7.50 – 7.35 (m, 12H). MALDI-ToF MS  $m/z$ : calc for  $\text{C}_{29}\text{H}_{16}\text{Br}_2\text{O}$ : 537.97; found: 537.77.

### GNR-precursor (1).<sup>14</sup>

The cyclopentadienone **2** (336 mg, 0.62 mmol) and diphenyl acetylene (100 mg, 0.33 mmol) were dissolved in *o*-xylene (5 mL). The solution was degassed sparging argon and then heated to 180 °C for overnight. After the mixture cooled down it was added to an excess methanol to precipitate the product as a white powder and then filtered through a PTFE. The powder was purified by column chromatography ( $\text{SiO}_2$ , cyclohexane: $\text{CH}_2\text{Cl}_2$  9:1) to yield the product as a yellowish powder (80 mg, 22% yield).  $^1\text{H}$  NMR (400MHz,  $\text{CDCl}_3$ , 298 K):  $\delta$ (ppm) 8.20 (d,  $J = 8.6$  Hz, 2H), 7.67 (d,  $J = 2.0$  Hz, 2H), 7.48 (dd,  $J = 8.7$ , 2.1 Hz, 2H), 7.19 – 7.12 (m, 6H), 7.07 – 7.02 (m, 4H), 6.95 – 6.86 (m, 6H), 6.76 – 6.66 (m, 4H).  $^{13}\text{C}$  NMR (101 MHz,  $\text{CDCl}_3$ , 298K):  $\delta$ (ppm) 142.00, 141.39, 140.00, 137.72, 133.01, 132.44, 131.98, 131.53, 130.44, 129.67, 128.44, 126.91, 126.87, 125.63, 124.63, 120.26. MALDI-ToF MS  $m/z$ : calc. for  $\text{C}_{42}\text{H}_{26}\text{Br}_2$ : 688.04; found: 688.03.

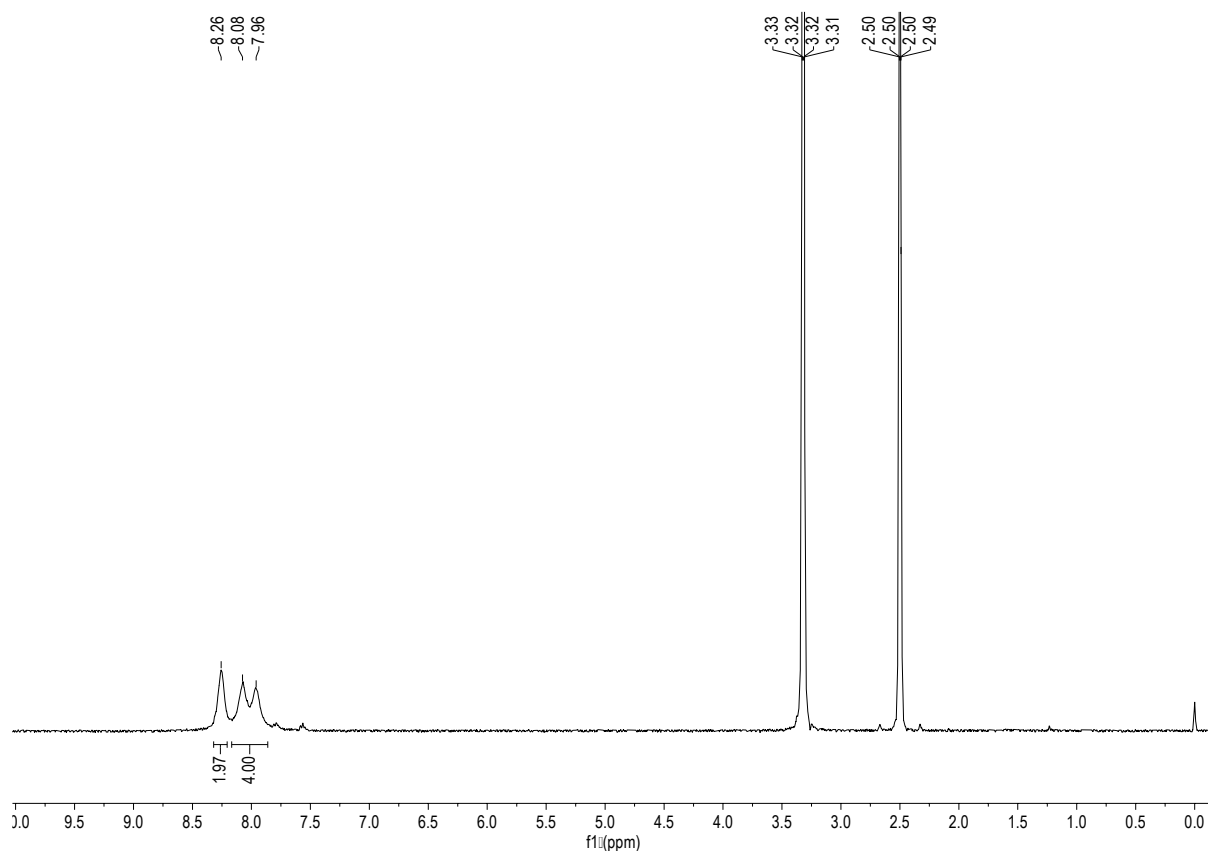


**Figure S9.**  $^1\text{H}$  NMR spectrum of 2,7-dibromophenanthrene-9,10-dione (**3**) in  $\text{DMSO-d}_6$ .

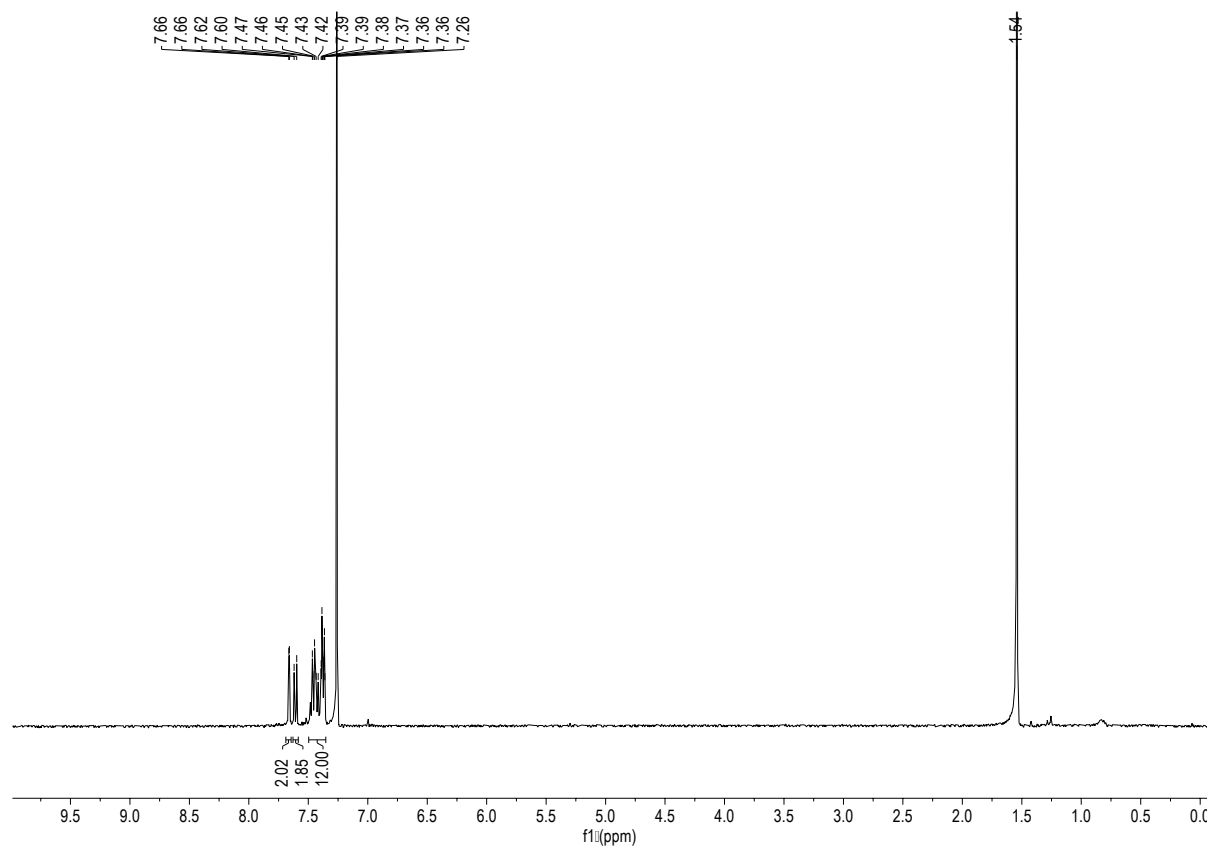


**Figure S10.**  $^1\text{H}$  NMR spectrum of the cyclopentadienone (**2**) in  $\text{CDCl}_3$ .

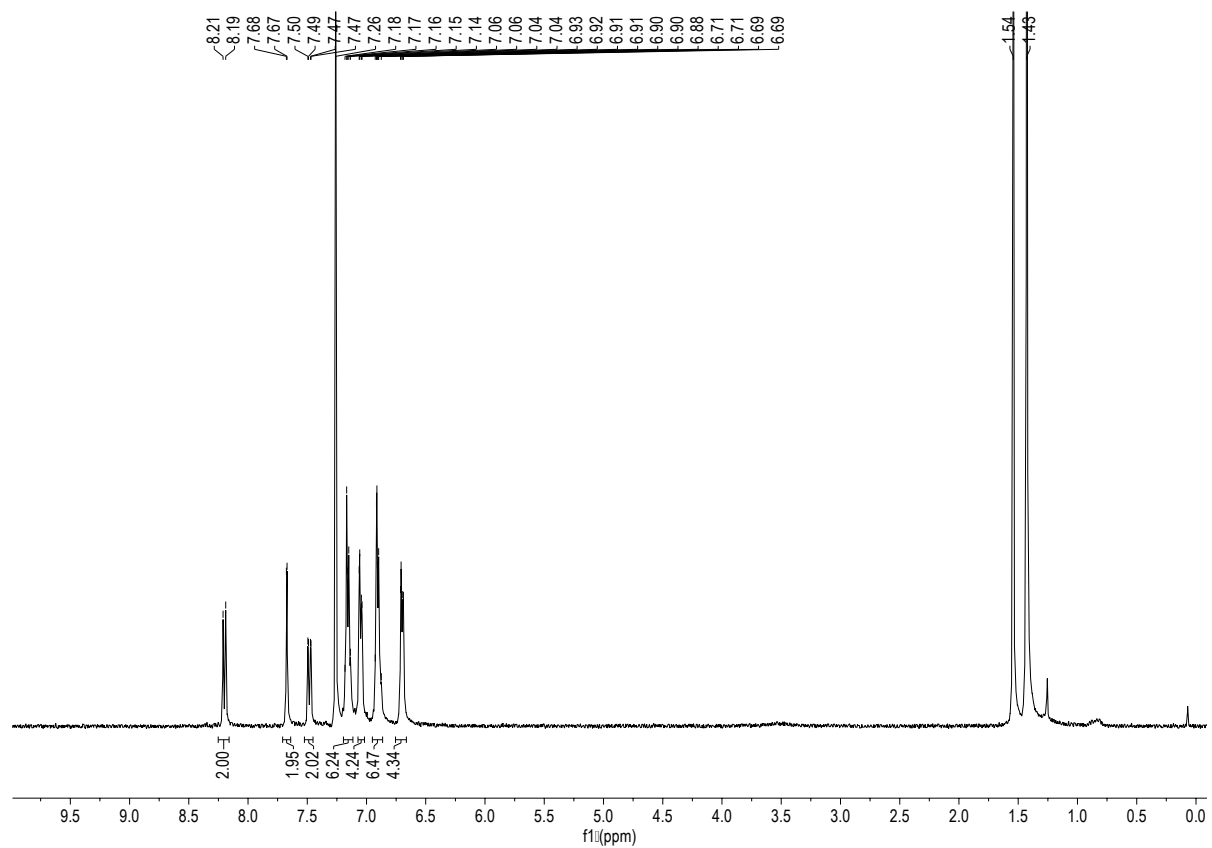


**Figure S11.**  $^1\text{H}$  NMR spectrum of GNR-precursor (**1**) in  $\text{CDCl}_3$ .

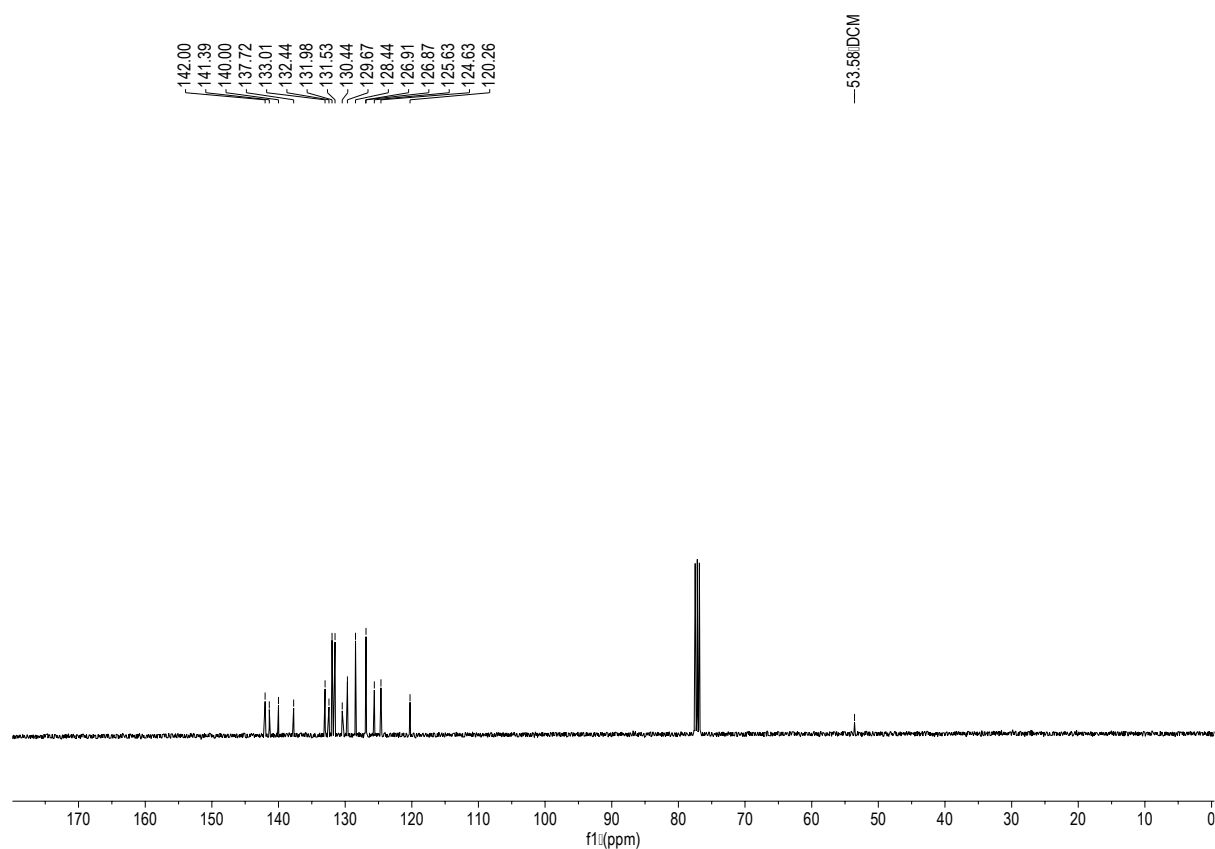


**Figure S12.**  $^{13}\text{C}$  NMR spectrum of GNR-precursor (**1**) in  $\text{CDCl}_3$ .

## References

- (1) Teeter, J. D.; Costa, P. S.; Zahl, P.; Vo, T. H.; Shekhirev, M.; Xu, W. W.; Zeng, X. C.; Enders, A.; Sinitskii, A. Dense Monolayer Films of Atomically Precise Graphene Nanoribbons on Metallic Substrates Enabled by Direct Contact Transfer of Molecular Precursors. *Nanoscale* **2017**, *9*, 18835-18844.
- (2) Galeotti, G.; Fritton, M.; Lischka, M.; Obermann, S.; Ma, J.; Heckl, W. M.; Feng, X.; Lackinger, M. Initial Coupling and Reaction Progression of Directly Deposited Biradical Graphene Nanoribbon Monomers on Iodine-Passivated Versus Pristine  $\text{Ag}(111)$ . *Chemistry* **2022**, *4*, 259-269.
- (3) Bronner, C.; Marangoni, T.; Rizzo, D. J.; Durr, R. A.; Jorgensen, J. H.; Fischer, F. R.; Crommie, M. F. Iodine versus Bromine Functionalization for Bottom-Up Graphene Nanoribbon Growth: Role of Diffusion. *J. Phys. Chem. C* **2017**, *121*, 18490-18495.
- (4) Cai, J. M.; Ruffieux, P.; Jaafar, R.; Bieri, M.; Braun, T.; Blankenburg, S.; Muoth, M.; Seitsonen, A. P.; Saleh, M.; Feng, X.; et al. Atomically Precise Bottom-Up Fabrication of Graphene Nanoribbons. *Nature* **2010**, *466*, 470-473.
- (5) Teeter, J. D.; Costa, P. S.; Pour, M. M.; Miller, D. P.; Zurek, E.; Enders, A.; Sinitskii, A. Epitaxial growth of aligned atomically precise chevron graphene nanoribbons on  $\text{Cu}(111)$ . *Chem. Commun.* **2017**, *53*, 8463-8466.

- (6) Linden, S.; Zhong, D.; Timmer, A.; Aghdassi, N.; Franke, J. H.; Zhang, H.; Feng, X.; Mullen, K.; Fuchs, H.; Chi, L.; et al. Electronic Structure of Spatially Aligned Graphene Nanoribbons on Au(788). *Phys. Rev. Lett.* **2012**, *108*, 216801.
- (7) Cai, J. M.; Pignedoli, C. A.; Talirz, L.; Ruffieux, P.; Sode, H.; Liang, L. B.; Meunier, V.; Berger, R.; Li, R. J.; Feng, X. L.; et al. Graphene Nanoribbon Heterojunctions. *Nat. Nanotechnol.* **2014**, *9*, 896-900.
- (8) Lukkien, J. J.; Jansen, A. P. J., CARLOS version 5.2, <http://carlos.win/tue.nl>; Eindhoven University of Technology, Eindhoven, **2009**.
- (9) Lukkien, J. J.; Segers, J. P. L.; Hilbers, P. A. J.; Gelten, R. J.; Jansen, A. P. J. Efficient Monte Carlo methods for the simulation of catalytic surface reactions. *Phys. Rev. E* **1998**, *58*, 2598-2610.
- (10) Bronner, C.; Bjork, J.; Tegeder, P. Tracking and Removing Br during the On-Surface Synthesis of a Graphene Nanoribbon. *J. Phys. Chem. C* **2015**, *119*, 486-493.
- (11) Mairena, A.; Baljozovic, M.; Kawecki, M.; Grenader, K.; Wienke, M.; Martin, K.; Bernard, L.; Avarvari, N.; Terfort, A.; Ernst, K. H.; et al. The Fate of Bromine after Temperature-Induced Dehydrogenation of On-Surface Synthesized Bisheptahelicene. *Chem. Sci.* **2019**, *10*, 2998-3004.
- (12) Thussing, S.; Flade, S.; Eimre, K.; Pignedoli, C. A.; Fasel, R.; Jakob, P. Reaction Pathway toward Seven-Atom-Wide Armchair Graphene Nanoribbon Formation and Identification of Intermediate Species on Au(111). *J. Phys. Chem. C* **2020**, *124*, 16009-16018.
- (13) Vo, T. H.; Shekhirev, M.; Kunkel, D. A.; Orange, F.; Guinel, M. J. F.; Enders, A.; Sinitskii, A. Bottom-up solution synthesis of narrow nitrogen-doped graphene nanoribbons. *Chem. Commun.* **2014**, *50*, 4172-4174.
- (14) Saleh, M.; Baumgarten, M.; Mavrinskiy, A.; Schafer, T.; Mullen, K. Triphenylene-Based Polymers for Blue Polymeric Light Emitting Diodes. *Macromolecules* **2010**, *43*, 137-143.